Stony Brook University

Title of Thesis

A Thesis Presented

by

Guanzhong Huang

to

The Graduate School

in Partial Fulfillment of the

Requirements

for the Degree of

Master of Science

in

Materials Science and Engineering

Stony Brook University

May 2015

Stony Brook University

The Graduate School

Guanzhong Huang

We, the thesis committee for the above candidate for the

Master of Science degree, hereby recommend

acceptance of this thesis.

Dr. Huolin Xin– Thesis Advisor
Staff Scientist, CFN, BNL

Dr. Balaji Raghothamachar – Second Reader
Research Scientist
Materials Science and Engineering Department.

Dr. Dilip Gersappe
Professor, Graduate Program Director
Materials Science and Engineering Department.

This thesis is accepted by the Graduate School

Charles Taber

Dean of the Graduate School

Abstract of the Thesis

Theoretical Investigation of Sub-lattice Imaging by 4-D In-line Holography

by

Guanzhong Huang

Master of Science

in

Materials Science Engineering

Stony Brook University

2015

In conventional annular dark-field scanning transmission electron microscopy, the beam rasters on a thin sample and the signal map by integrating the transmitted electrons with an annular shaped detector in the diffraction space. Because the scattering cross sections for high-angle scattered electrons is proportional to the atomic number square. The resulting image has a so called Z-contrast. Z-contrast images can give atomic resolution images of atomic columns however it has an inherent problem—light elements buried in the tails of the heavy elements containing columns. In this thesis, we propose to use a pixelated a 2-D imaging detector to record the full CBED pattern at each beam position. This position-dependent coherent CBED map allows scattering intensities to be digitally integrated or subtracted from any parts of the diffraction space. In principle, if there is no noise, it can replace all detectors inside the microscope. The coherent CBED mapping data (x-y-k_x-k_y, namely 4-D inline holography) can also be used to achieve symmetry dependent sub-lattice imaging. For example, in ABO_3 systems,

it is possible to design an optimal transformation matrix (i.e. an digital detector function $D(k_x,k_y)$) to specifically image scattered electrons from A site cations only. The detector function can be further optimized to improve the signal-v.s.-thickness linearity. This problem can be mapped to a matrix inversion problem. Due to the size of the problem, it is more efficient to use data mining to construct an initial guess and then use conjugate gradient method to search for the best solution. Accomplishing this technique gives unique capability in imaging light elements, for instance measuring the degree of charge of lithium ion battery electrodes.

Keywords: TEM, STEM, CBED

Dedication Page

To my parents

Table of Contents

List of Figures

List of Tables

List of Abbreviations

TEM – Transmission electron microscopy

STEM –Scanning transmission electron microscopy

ADF—Annuldar dark field

ABF—Annuldar bright field

BF—Bright field

EELS—Electron energy loss spectroscopy

DPC—Differential phase contrast

Preface

Science is a tough journal, but I will guide you through it.

Acknowledgments

I want to give my special thanks to my advisor, Dr. Huolin Xin. I am deeply grateful for his selfless guidance, help, and time.

Chapter 1

Introduction

1. Scanning Transmission Electron Microscopy

1.1 Annular dark-field Scanning Transmission Electron Microscopy (ADF-STEM)

A scanning transmission electron microscope (STEM) is conceptually simple. A high-energy electron beam (100-300KeV) is focused by a magnetic lens down to a very small spot on an electron transparent sample (Fig. 1a). The beam is scanned and the scattered electrons are recorded to build up a two dimensional image. This is very similar to a scanning electron microscope (SEM). However, instead of collecting the secondary and back-scattered electrons as is done in the SEM, the transmitted electrons are recorded in reciprocal space by an annular dark field (ADF) detector. Because the electron scattering cross section for high-angle scattering is roughly proportional to the square of the atomic number of the target atom (Rutherford scattering), ADF-STEM is known to give images with atomic-number contrast (Z-contrast).

In SEM, a bulk sample is imaged, and thus the imaging resolution is typically limited by the average range of electron implantation rather than the size of the probe unless substrate with very low secondary electron yield is used. In the high resolution STEM, only very thin samples (several nanometers to several hundred nanometers in thickness) are used and the resolution is limited mainly by size of the focused electron probe.

The wavelength of a 200KeV electron is 0.025 Å. If we had an ideal lens, we would be able to focus the electron beam down to a hundredth of an angstrom. However, a round magnetic lens

always has spherical aberrations, causing rays far from the optical axis to focus at a different point than the paraxial rays. Therefore, to achieve optimal resolution, an aperture is introduced to reject electrons far from the optical axis. The typical optimal aperture size used in a 200-KeV STEM is 9.6mrad giving a 1.6 Å resolution. Recent development of aberration correctors enables the aperture to be opened which greatly increases the resolution of STEM. A PRL paper [1] in March of this year reported the resolution of 47pm-spaced Ge [411] dumbbells in a 300 KeV aberration-corrected STEM. STEM, especially with aberration correctors, has become an increasingly powerful tool to probe atomic and sub-atomic physics in materials.

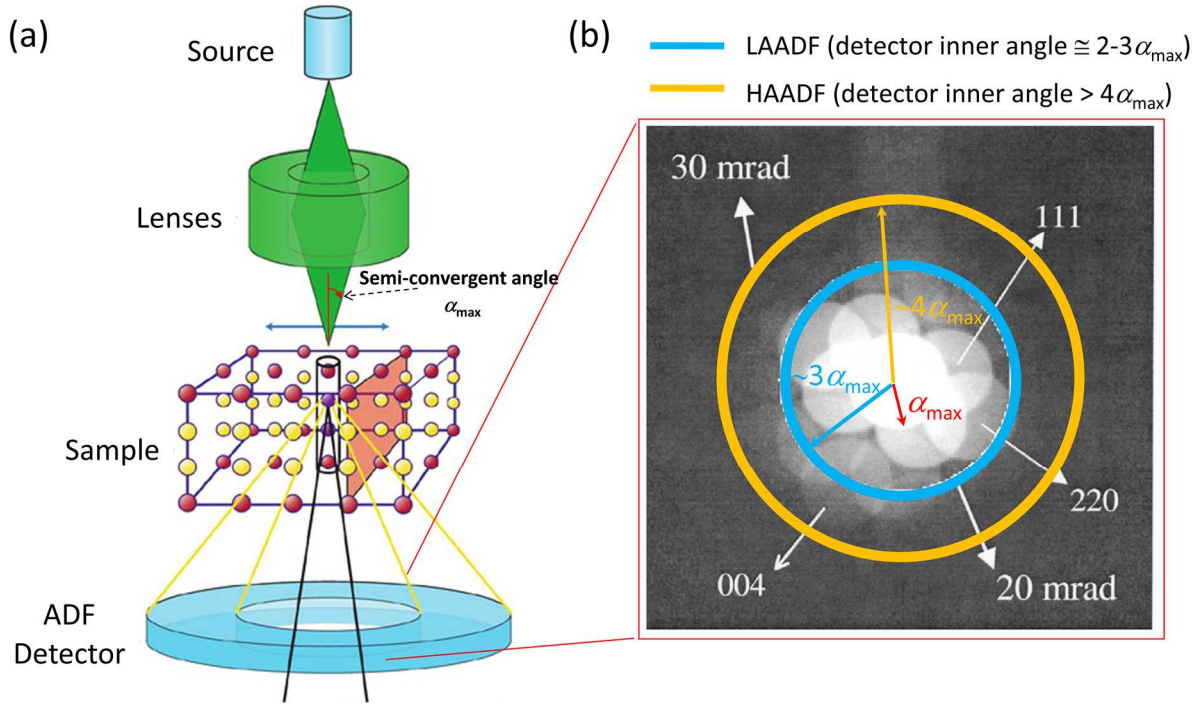

Figure 1. (a) A schematic diagram of the annular dark-field scanning transmission electron microscope; (b) an experimental CBED pattern of Si [110] (100KeV, α_{max} = 7.6mrad) with the ~3α_{max} and ~4α_{max} circle overlaid (figures adapted from ref [1] and [2]).

The signal in an ADF-STEM image comes from the high-angle scattered electrons. However, these electrons are only a small fraction of the incident beam. Therefore, we are facing the same problem that most experimental physicists have been fighting for decades: to detect low signal with less noise. There are two ways to tackle this problem in STEM. First, we can design an efficient detector to enable single electron detection. Second, we can improve the geometry of the detector. In order to achieve better counting statistics, we want more electrons to be recorded. However, spatial contrast is lost if all the electrons are collected. However, if we could build a large detector consisting of several segments, we can potentially combine the signals from different segments in a proper way to achieve unique contrast and better SNR.

1.2. Annular bright-field Scanning Transmission Electron Microscopy (ADF-STEM)

One of the shortcomings of ADF-STEM is that it is not particularly sensitive to the lighter elements in the samples. For examples, in SrTiO3, oxygen columns does not show up in the ADF-STEM images. This gives an incomplete characterization of the atomic structure of materials. To mediate this problem, annular bright-field imaging (ABF-STEM) has been developed. In this imaging mode, an annular shaped detector is designed such that the outer edge is slightly larger than or equal to the bright disk and the inner edge is smaller than the bright disk. The resulting image would have a coherent bright field contrast, i.e. the contrast is sensitive to defocus and samples thickness. However, at the focus where the ADF-STEM image is perfectly infocus, the ABF image gives a directly interpretable contrast. A negative dip can be seen at the position where the atomic columns sit and light element columns would clearly show up in this infocus image. This imaging mode has been applied to the imaging of oxygen octahedra tilts

multiferroic materials, and other light elements such as hydrogen in metal hydrides, and lithium and metal oxides.

1.3 Differential phase contrast – Lorentz STEM

In a modern field emission gun scanning transmission electron microscope, phase contrast is very easily discerned by the bright-field detector (the illumination cone is magnified by the post specimen lens to be much bigger than the detector) due to the high available current. Differential phase contrast is rarely used for high-resolution imaging. However, differential phase contrast is sensitive to very small change in phase [3]; thus, it could be used to image contrast from different magnetic domains which is known to be Lorentz STEM[4].

Imagine there was a weak sinusoidal phase grating, $\phi(x) = \phi_0 \sin(2\pi x/L)$ ($\phi_0 << 0$). After the electron probe is scattered from this grating, the diffraction pattern showing on the detector plane should be three cones (Fig. 4). The central cone is the unscattered wave. The cones on the two sides are the diffracted beam. The two overlapped areas are where the interference takes place. However, the intensity modulations in these two areas are in opposite sign. If the detector collects the whole bright-field cone, no phase contrast is preserved. If we subtract the right quadrant from the left quadrant, the phase contrast is recovered and the amplitude contrast is eliminated. The collected phase contrast is a phase $\pi/2$ shifted from the original modulation ($\sin x \rightarrow \cos x$). Therefore, this contrast reflects the differentiation of the actual phase modulation. Using the quadrant detector, the differential contrast in both x and y directions can be obtained.

Upon the solid quadrant detector design, Chapman et al in 1990 proposed an eight segments design[4]. It preserves the four center quadrants and added four more segments to form an

quandrant + annular detector (Fig. 4b). If we defined κ to be the ratio of the inner angle to the angle of the bright-field cone, the quadrant detector is the $\kappa = 0$ case. Chapman designed the eight-segment detector mainly trying to eliminate the non-magnetic contrast from the differential-contrast images. With an increase κ, the mid-band information is significantly reduced (shown in Fig. 5), whereas the high and low frequency information is rather intact. This could potentially reduce some of the crystallite contrast in magnetic materials.

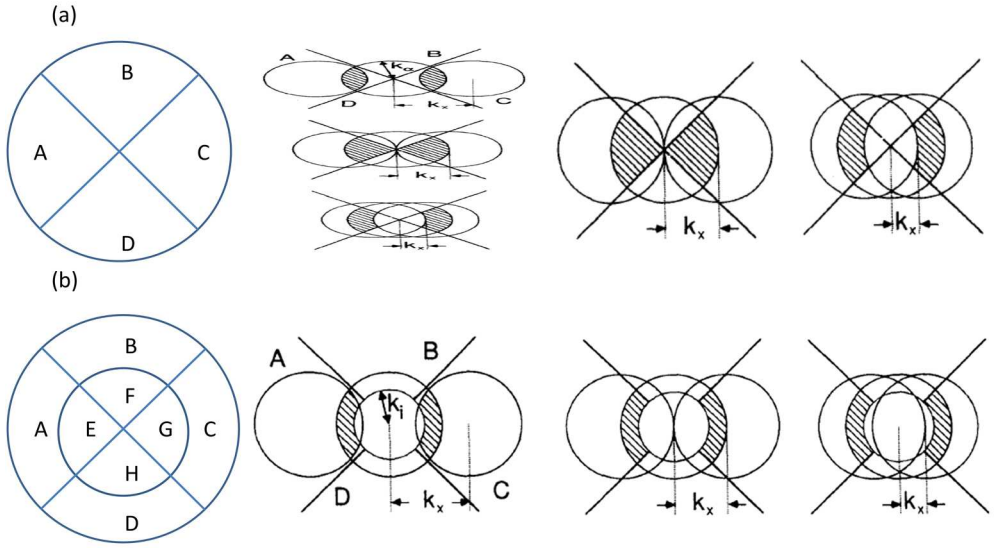

Figure 2. (a) The solid quadrant detector: the electron intensity distribution in the plane of a solid quadrant detector arising from weak phase sinusoids of three different periodicities. The information carrying signals arise only from the hatched areas; (b) the eight segment detector. (figure adapted from ref [4])

Aharanov and Bohm showed that the phase shift on the incident electrons resulted from a magnetic field is

$$\nabla\phi = -\frac{\pi et(\boldsymbol{B} \times \boldsymbol{n})}{h}$$

Where $\boldsymbol{B}$ is the magnetic field, $\boldsymbol{n}$ is the unit vector along the trajectory the electron travels and t is the specimen thickness. Therefore, the in-plane magnetic field gives rise to the phase gradient. Using the Chapman's eight-segment detector, this magnetic originated phase gradient could be imaged. In Chapman's paper (200KeV, α_{max} = 0.5mrad, probe size ≈ 50nm), he pointed out that if only the signal from the inner quadrants is used (E-G), the image mainly reflects the contrast from the crystallites but not the magnetic originated structure. However, while using only the outer segments, even though fewer electrons are counted, the images show a very clear magnetic originated signal. A simple argument about why the contrast is different from the inner and outer segments is as follows. The magnetic field in each magnetic domain results in a small deflection of the beam. It is typically on the order of 100 μrad for the magnetic specimens of interest. This small deflection is in the reciprocal space; thus it is small shift of the bright-field cone in the detector plane. Following this argument, the introduction of a hole in the detector has no effect on the magnetic originated signal. Furthermore, the introduction of the hole should also increase the SNR of the magnetic originated signal similar to the Zernike phase plate.

Above we have shown that an eight-segment detector could produce differential phase contrast and by selecting the outer segments, the non-magnetic originated signal could be reduced and the magnetic originated signals could be recorded with better signal to noise ratio.

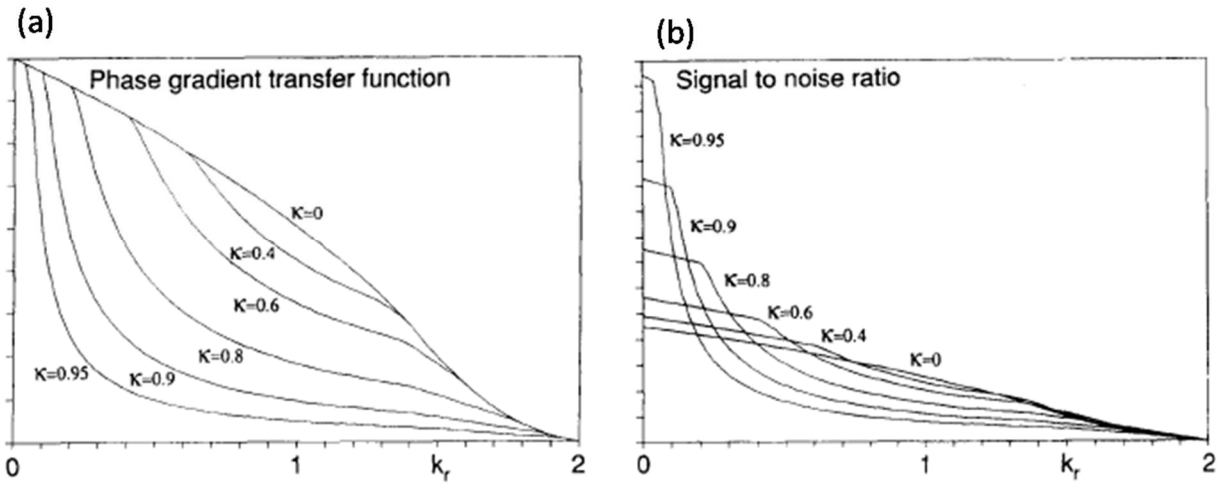

Figure 3. (a) Variation of the phase gradient transfer function with reduced spatial frequency for detectors with different values of κ; (b) variation of the signal to noise ratio with reduced spatial frequency for detectors with different values of κ (figure and caption copied from ref [4])

1.4 Auto-grain-segmentation enabled STEM imaging

Due to the continued scaling of the front-end device feature size in VLSI, the RC delay of back-end copper interconnects has become a major bottleneck. Therefore, the knowledge of the grain size distribution in interconnecting copper wires is of great importance to the semiconductor industry because the wire resistivity is highly dependent on grain size. Even though the grain-grain contrast could be picked up in BF-S/TEM images, there is currently no effective algorithm that could automatically and reliably segment grains in BF-S/TEM images. Human hand-tracing the grain boundaries is the only reliable way to approach this problem. However, it requires a lot of man power and it is a painful process. Therefore, an imaging mode that could allow automatic grain segmentation would be of great impact in this field.

Caswell et al [5] used the prototype PADs and in doing so, successfully demonstrated the auto segmentation of nanoscale grains in copper. The algorithm is relatively simple. Because the diffraction pattern at each scanned pixel is recorded by the PAD, a diffraction pattern cross-correlation of next-nearest neighbor could be carried out in both the vertical and the horizontal directions. The pixel-by-pixel product of the two cross-correlation map could illustrate all the grain boundaries. This final product with some smoothing provides enough contrast without ambiguity that could be auto-segmented by Image-J.

2. A highly efficient annular dark field detector

Fig. 1b shows the diffraction pattern a convergent 100KeV electron beam with a semi-convergent angle of α_{max} = 7.6 mrad along the Si [110] zone axis. The annular dark-field detector is placed in this projected Ewald-sphere-cut reciprocal space. To record directly interpretable Z-contrast images, it is generally recommended that the detector inner angle to be bigger than any visible disks to avoid diffraction contrast. This imaging mode is called high-angle annular dark-field (HAADF)-STEM. Diffraction contrast is useful when strain fields or contrast between different grains is needed. In this case, the inner angle of the detector should be small enough to cover some visible diffraction disks. This imaging mode is referred as low-angle annular dark-field (LAADF)-STEM. Therefore, the choice of the detector inner angle is imaging mode, beam energy, convergent angle and zone axis dependent.

The general rule of thumb is that the inner angle is around 2-3 times the convergent angle for LAADF and bigger than 4 times the beam convergent angle for HAADF. This rule is suitable for aberration-uncorrected high resolution STEM. The nice thing about electron microscope is that

the diffraction pattern can be magnified or demagnetized by post specimen projection lenses. Therefore, with a fixed-size detector, the inner angle of the detector with respect to the convergent beam diffraction pattern (CBED) can be changed continuously. The only concern is that we want the outer angle of the detector to be as big as possible to collect all the forward-scattered electrons and to ensure that the imaging is incoherent.

The physical size of the detector is limited by the size of the column. The limited size of the detector will result in a decrease of SNR and contrast reversal in imaging thick samples. We will further discuss how to solve this problem in section 3. Below, we will describe the physical design of an efficient annular dark-field detector to enable single electron detection.

Most modern commercial ADF detectors are based upon the design of Kirkland and Thomas in 1996 [6] with slight modifications. So, we will focus on describing the Kirkland and Thomas ADF detector.

The innovation of the Kirkland and Thomas's new design is to replace the inefficient detector provided by the electron microscope manufacturer. Fig. 2 shows a cross section diagram of Kirkland-Thomas (KT)-detector. The old detector is similar in cross section to the KT-detector. The main improvement over the old detector is the replacement of an inefficient light guide and a plastic scintillator by a quartz light pipe and a robust yttrium aluminum perovskite (YAP) scintillator. KT reported that initial tests indicate KT-detector is 100X more efficient than the old detector. Below we will describe each part of KT-detector in detail.

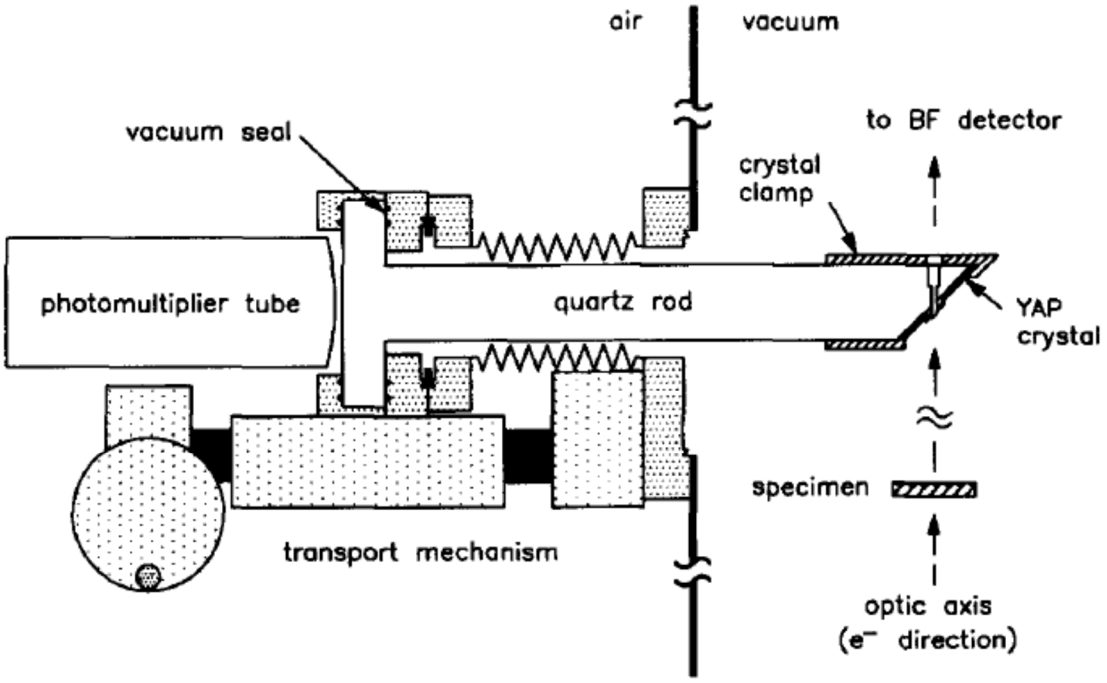

Figure 4. Cross section diagram of the new detector. The light from a single crystal YAP scintillator inside the vacuum is coupled to a photomultiplier tube outside the vacuum using a solid quartz light guide (figure and caption adapted from the classic paper by Kirkland and Thomas [3]).

2.2 Scintillators

The old detector uses plastic scintillator (NE160) to convert collected electrons into photons that are amplified by a photomultiplier (PMT). The plastic scintillator has an extreme fast response time (2.3ns) and is widely used in nuclear physics experiments. However, the electron dose in an electron microscope is orders of magnitude higher than that in the nuclear physics experiments. So, any accidental placement of the full beam on the plastic scintillator will result in a permanent damage of the illuminated area (unavoidable during the installation and initial alignment of the microscope). The available choices in terms of long damage lifetime are yttrium aluminum

garnet (YAG) and yettrium aluminum perovskite (YAP). They both have an electron conversion efficiency roughly twice that of plastic scintillator (shown in Tab. 1). Their response time is relatively fast (70 ns for YAG and 30 ns for YAP) and they are both able to withstand the high temperatures incurred during a bake out of the microscope. The main difference for these two scintillators is that YAG has a peak emission at a wavelength of 550nm and YAP at 370nm. YAG's peak emission wavelength matches the extended red multialkali PMTs or CCD detector. However, it does not match the maximum sensitivity of a normal photomultiplier (type 8575 bialkali PMT with a peak sensitivity near 400nm supplied with VG HB-501A STEM). Therefore, YAP was chosen for KT-detector.

Kirkland and Thomas chose a single crystal over powder because a single crystal could provide a smooth polished surface for uniform aluminum coating to avoid charging on the scintillator. Kirkland and Thomas found that the use of P-47 powder could result in islanding of coated aluminum which leads to regional charging and hence deflect the beam. Furthermore, powdered scintillators tend to have a spatially non-uniform sensitivity which is undesirable when diffraction contrast is recorded. Additionally, KT found the use of YAG powder could suppress the very long tail of the spectrometer point spread function of electron energy loss spectrometers. The manufacturer of commercial electron energy loss spectrometers uses single crystal YAG with an anti-reflection coating to reduce the tail, but theoretically it should be a little bit worse than YAG powder. Albeit, ADF detector is an area detector where no spatial resolution is required. Therefore, the choice of single crystal is superior to powder.

Table 1 Scintillator data from KT's paper [6]

	Plastic (NE160)	**YAG**	**YAP**

Damage lifetime (h/50nA)	0.9	$>10^4$	$>10^4$
Energy efficiency (%)	3	4	7
Photons per 100 keV electron	1000	1800	2100
Emission wavelength (nm)	423	550	370
Emission photo energy (eV)	2.93	2.26	3.35
Decay time (ns)	2.3	70	30
8575 photomultiplier DQE	0.24	0.07	0.25

2.3 Coupling between the scintillator and the photomultiplier

The old detector uses an internal surface polished hollow tube as a light guide from the scintillator to the PMT. There is 65mm vacuum gap between the end of the tube and the type 8575 PMT (bialkali photocathode). The gap contains a leaded glass, a vacuum window and the space for the detector to retract. This vacuum gap could potentially allow the light to escape and the stray light to come in which increases the noise level.

The light guide used the KT-detector is a solid rod made from a single piece of quartz. The quartz rod is coated with 300nm-thick aluminum except for the two ends. The end of the quartz rod is sealed by a double O-ring. The entire assembly is enclosed by a UHV bellows to allow the retraction of the detector. Because the PMT has a larger diameter than the longer portion of the quartz rod, the loss of light is negligible. The scintillator is clamped to the end of the rod by aluminum housing. Gluing the scintillator to the quartz was not considered because it may cause problem during bake out due to the difference in expansion coefficients of two materials. In addition, any future replacement of the scintillator is convenient with a clamp mechanism. The thickness of the YAP scintillator is 2mm to ensure the mechanical strength during installation. However, a 0.5mm YAP scintillator could be used to reduce self-absorption. The top surface of the scintillator facing the beam is polished and coated with 100nm-thick aluminum to reduce

charging and reflect light back to the light guide. The surface close to light guide has a mat finish which improves the coupling to the light guide.

2.4 Calculation of the efficiency of the KT-detector

KT-detector replaced the plastic scintillator and the hollow-tube light guide in the old detector with a single crystal YAP scintillator and an aluminum-coated quartz rod. Each component gives approximately a factor of 10× improvement in efficiency over the original design. We will go through the calculation for the KT-detector below.

The detector efficiency can be calculated using the data in reference [7] (reproduced in Fig. 3). The length of the quartz light guide is 8.7 inch. From the curve b in Fig. 3, we can estimate the efficiency of the light guide to be $\varepsilon \approx 5/10 = 0.5$. The three surfaces at the PMT and the ends of the light guide give a damping factor of 0.95^3. The self absorption of the scintillator yields another factor of 0.7. Combining the three numbers gives the total efficiency of the KT-detector $\varepsilon_{KT} = 0.5\times0.95^3\times0.7= 0.3$. A single 100KeV electron could generate 2100 photons in the scintillator and 630 of them could be transmitted to the PMT. The quantum efficacy of the PMT is 0.25. It means a single electron could generate about 160 photoelectrons in the PMT. PMT with bialkali photocathode is known to have a very low dark-current. Therefore, KT-detector produces a SNR of 12.6 for single electron counting. On the other hand, if we go through the same calculation for the old detector, we find a single electron could only produce approximately one photoelectron in the PMT. The readout dark count spectra for this PMT is peaked at one photoelectron. Therefore, the old detector is not feasible for single electron detection.

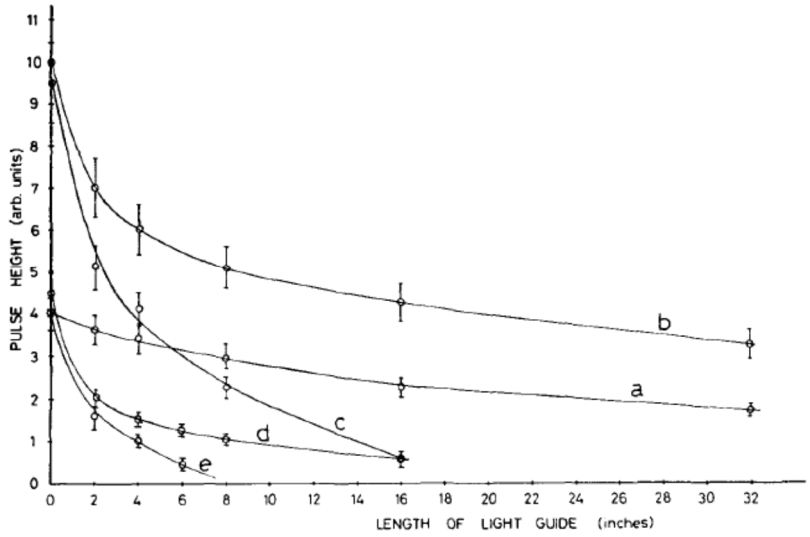

Figure 5. Variation of pulse height with length of light guide for various reflective wrappings. (a) Total internal reflection only, (b) total internal reflection with reflective covering, (c) surface of light guide painted with NE 560 reflector paint, (d) specular reflector without light guide, (e) diffuse reflector without light guide. (figure and caption adapted from Ref [7])

2.5 Summary

The efficiency of an annular dark-field detector mainly depends on the choice of the scintillator, the light guide and photomultiplier. Damage life time is a major concern for scintillator used in electron microscope due to the extremely high beam current. P47 phosphor ($Y_1Si_2O_7$:Ce3+; yttrium silicate activated with cerium), YAG, YAP and the newly developed LuminiX ScintillatoR (LXSR) are suitable choices. Photomultipliers with bialkali photocathode well match with P47, YAP and LXSR, but CCD and multi-alkali photocathode matches YAG. Generally speaking reflective coated quartz is the best choice for light guide. The diameter of longer portion of the light guide need to be smaller than the diameter of the active area of the

PMT is another important design rule. Powder vs. single crystal and gluing vs. clamping are practical things to be considered for specific applications.

3. An ideal STEM detector—direct detection pixelated detector

Most current STEMs are equipped with two detectors: one annular dark-field detector and one bright field detector. They enable a STEM to simultaneously acquire ADF images with directly interpretable mass-contrast and BF images with phase and diffraction contrast. However, there are certain cases in which this configuration fails to provide information we need that is actually encoded in the transmitted electrons. The main problem here is that both the ADF and BF detector are area detectors losing the rich information in the convergent beam electron diffraction (CBED) pattern. Therefore, if we can record the whole CBED pattern on each scan pixel, we will be able to extract the spatial dependent map about a certain encoded information by post processing. For example, if we sum all of the counts of on the peripheral pixels, we essential get back the ADF signal.

A charge-coupled device (CCD) is generally used to record high resolution diffraction patterns in most electron microscopes. However, a CCD cannot be used to directly collect high energy electrons. A phosphor screen coupled to the CCD by fiber optics is used to convert energetic electrons into photons. The CCD camera for an electron microscope is bulky and expensive. The biggest problem with this device is the frame time of CCD is way slower than the typical pixel dwell time used in STEM (TV rate vs. 0.1 MHz). Phosphor is also known to have a fat point spread function and the exhibit the problem of afterglow. Therefore, it is not optimized for high-speed acquisition and high beam current application in STEM.

Caswell et al [5] recently showed that pixel array detectors (PADs) originally designed for image X-ray could be used to directly record STEM CBED patterns with very fast read out speed. Each pixel of PADs consist of a PIN photodiode and each photodiode is directly connected to an application-specific integrated circuit (ASIC) pixel to directly integrate charged into voltage by a simple op-amp integration unit. No mechanical shutter is required because the exposure time is set by the electronic shutter of the integrator. When the PADs is being operated, the photodiodes are highly reverse biased to increase the internal electric field to flush electrons and holes -- generated by an incident high energy electron -- to separate ends before they recombine. In their PADs, the photodiode is 150 um wide and 300 um deep. It is shown that 99% of the electrons are deposited inside the pixel for 120KeV electron beam, whereas 200 KeV electrons deposit a significant amount of electrons in to neighbor pixles. This problem could be potentially solved by making larger pixels. The measured SNR for a single 120KeV electron for this PAD is roughly 2. This rather low SNR was due to limitation of the external support hardware and the fact that the dark count of this device is not specially optimized for room temperature operation. However, this PADs is only a prototype detector that has not been fully optimized for high energy electron detection. A recently developed mixed mode PAD could be adapted to electron detection as well. It is predicted that it has a single electron SNR of more than 20[8].

Thus, it is shown that the high-speed pixel array detectors could be well adapted to the recording of high energy electron diffraction pattern with an acquisition rate that typical STEM image acquisition. Below we will discuss several applications in which the PADs are uniquely poised to provide the necessary information for full image interpretation

Chapter 2

Results

1. Coherent beam CBED mapping

In conventional annular dark-field scanning transmission electron microscopy, the beam rasters on a thin sample and the signal map by integrating the transmitted electrons with an annular shaped detector in the diffraction space. Because the scattering cross sections for high-angle scattered electrons is proportional to the atomic number square. The resulting image has a so called Z-contrast. Z-contrast images can give atomic resolution images of atomic columns however it has an inherent problem—light elements buried in the tails of the heavy elements containing columns. Here we use a pixelated a 2-D imaging detector to record the full CBED pattern at each beam position. This position-dependent coherent CBED map allows scattering intensities to be digitally integrated or subtracted from any parts of the diffraction space. In principle, if there is no noise, it can replace all detectors inside the microscope. The coherent CBED mapping data (x-y-k_x-k_y, namely 4-D inline holography) can also be used to achieve symmetry dependent sub-lattice imaging. For example, in ABO_3 systems, it is possible to design an optimal transformation matrix (i.e. an digital detector function $D(k_x,k_y)$) to specifically image scattered electrons from A site cations only. The detector function can be further optimized to improve the signal-v.s.-thickness linearity. This problem can be mapped to a matrix inversion problem. Due to the size of the problem, it is more efficient to use data mining to construct an initial guess and then use conjugate gradient method to search for the best solution.

Accomplishing this technique gives unique capability in imaging light elements, for instance measuring the degree of charge of lithium ion battery electrodes.

1.1 Data acquisition

The data was acquired in a 200 keV aberration corrected S/TEM as shown in Figure 6. The convergence semi-angle of the beam was set to 28 mrad. The CBED pattern at each beam position was recorded by a scintillator coupled CCD at a frame rate around 10-20 frames/second. The beam and the CCD are software synchronized through the Gatan software. Exposure time of each CBED pattern is 0.1 second.

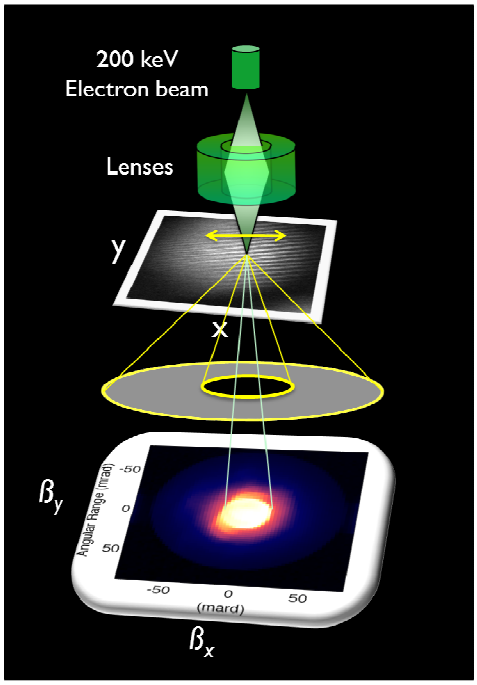

Figure 6. The setup for coherent CBED mapping.

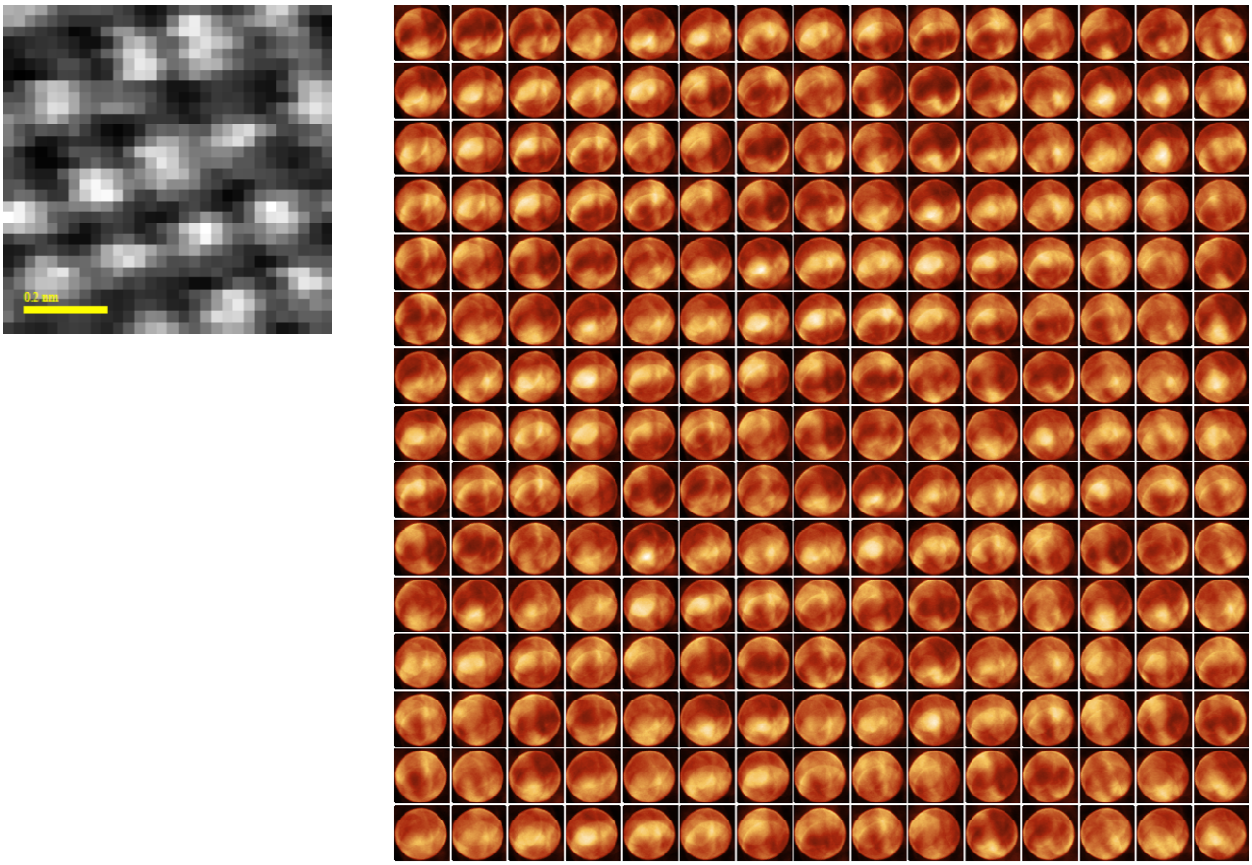

Figure 7. CBED mapping results. (a) the simultaneously acquired ADF image. (b) the CBED patterns matrix; only the center bright disk is shown.

The results is presented in figure 7. As one can see, that where the is no atom, the center intensity of the bright disk is higher and vice versa. This is consistant with the contrast you will see from bright-field STEM (BF-STEM) images. Figure 8 shows the out of focus CBED mapping. This result can be used for ptychography reconstruction of materials. It is worth noting that, inelastically scattered electrons, particularly those that have lost very little energy, would preserve the elastic contrast. As demonstrated in Figure 9, this is indeed the case. The CBED mapping formed by electrons that have lost 25 eV of energy form the same patterns as these of the elastically scattered electrons.

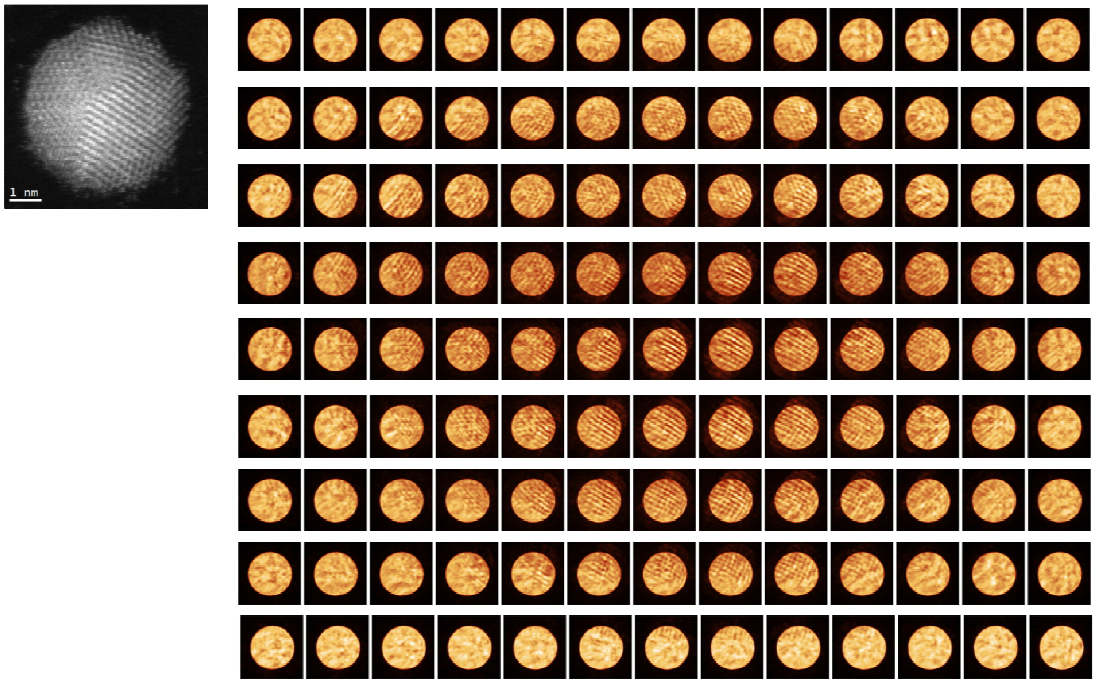

Figure 8. Out of focus CBED mapping of the particle shown in the inset.

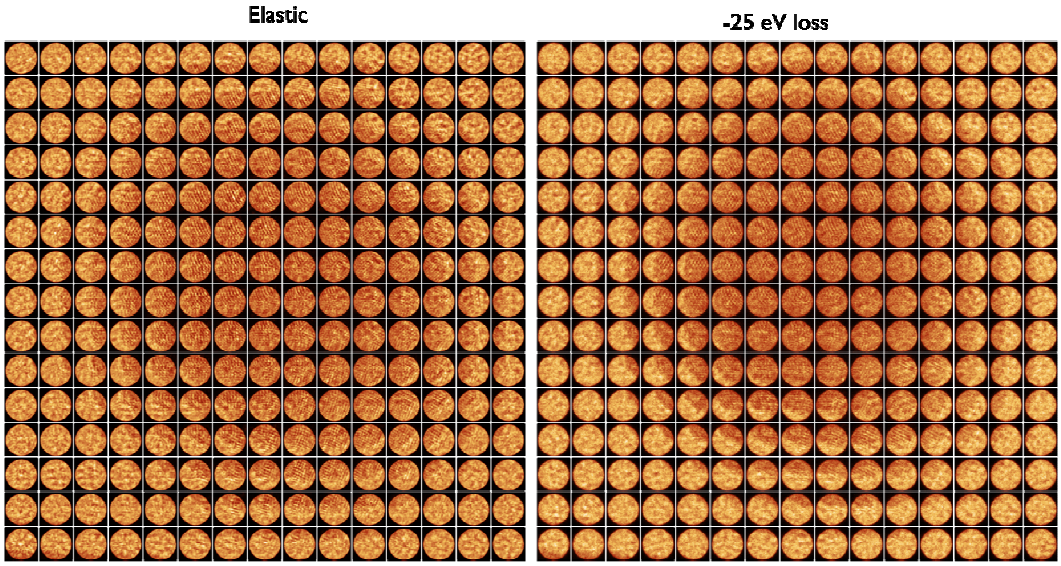

Figure 9. The comparison of the CBED pattern formed by the elasticallyscattered electrons and those that have lost 25 eV.

1.2 Digital detector response function

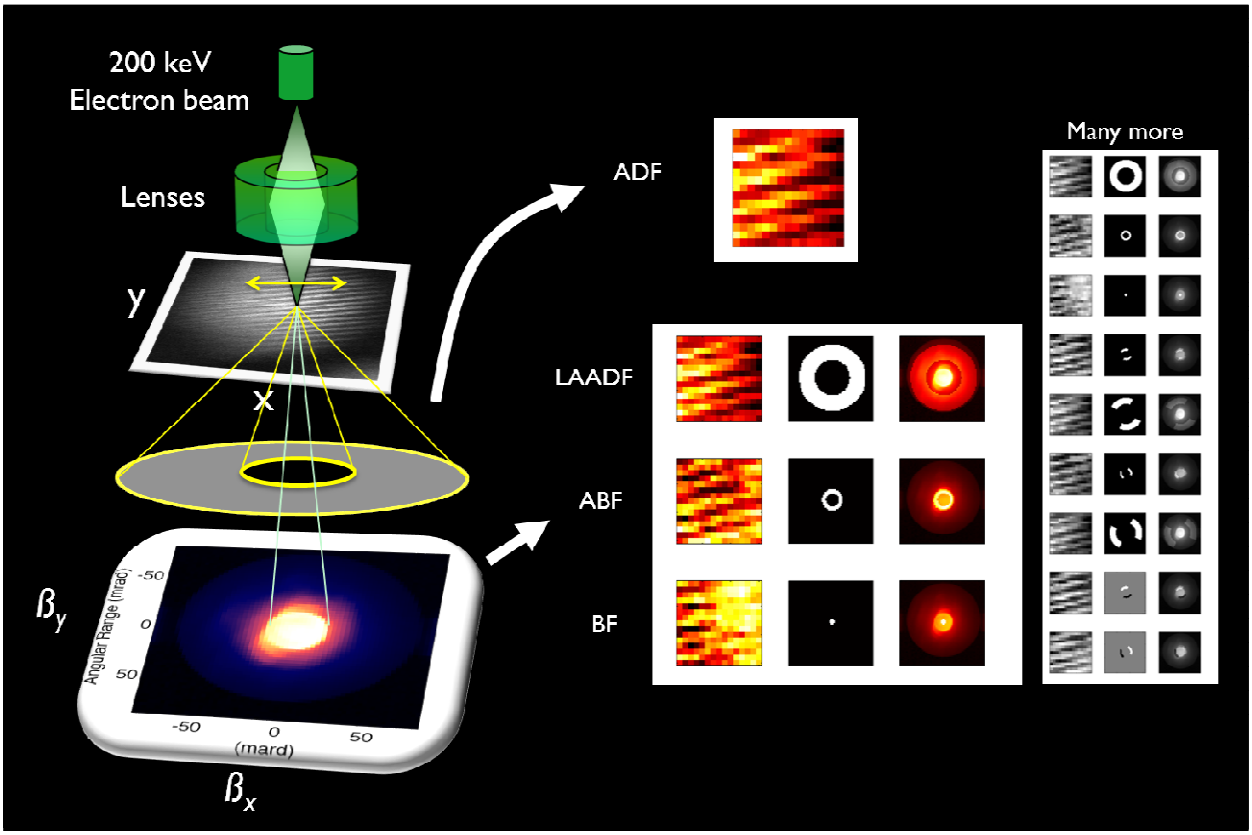

Figure 10. By applying digital detector response functions, images can be formed.

Because the CBED pattern from each position is capture by the pixelated detector (CCD here), a digital detector response function can be applied to each pattern to form a gray scale image. As shown in Figure 10, low angle annular dark field images or differential phase contrast images can be formed by engineering these detector response functions.

2. Detector response function engineering for sub-lattice imaging

2.1. Simulation of STEM CBED patterns of [001] $SrTiO_3$

Figure 1 shows the simulated STEM CBED patterns from specified locations on a SrTiO3 structure. It shows that there are considerable difference in the ZOLZ pattern as the beam move to different locations on the lattice.

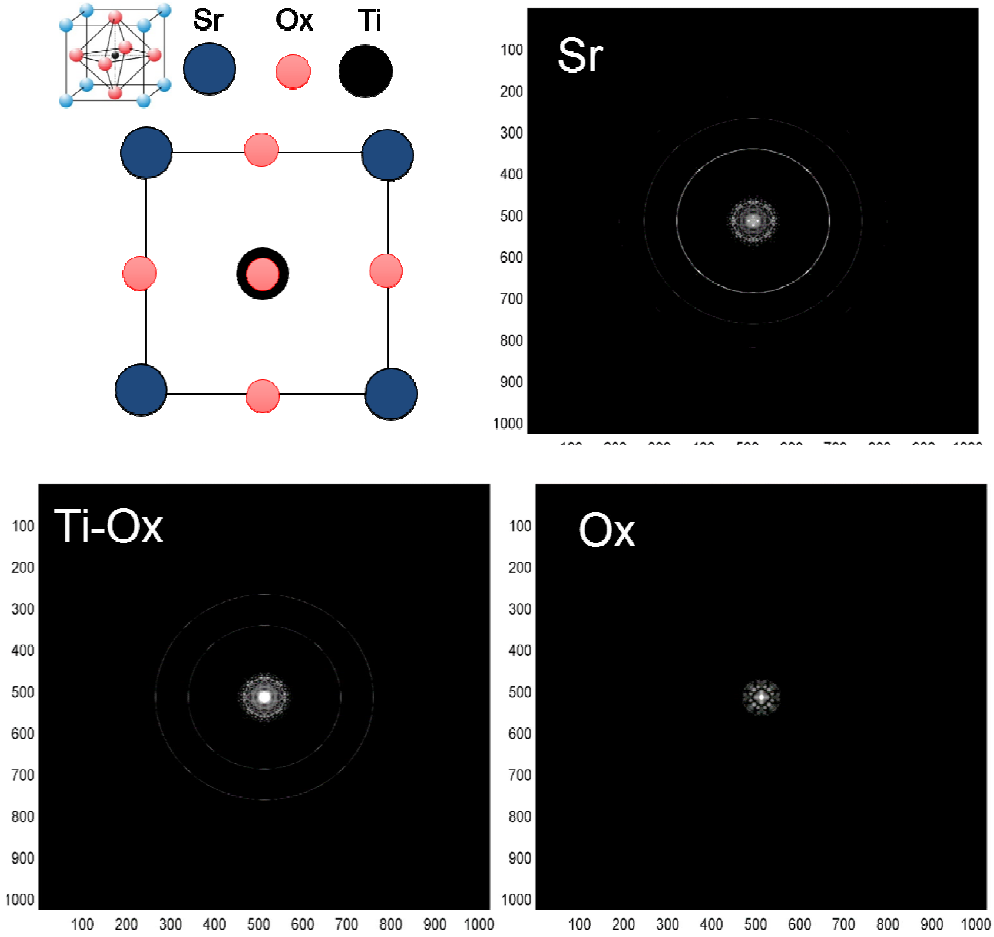

Figure 11. The simulated CBED pattern of a convergent STEM beam when it is located on the Sr, Ti-O, and Ox columns respectively. Simulated by multilsice code by Earl Kirkland.

Inspired by the fact that there is an obvious spatial correlation with the CBED pattern, one can explore the possibility to use the x-y-kx-ky 4-D data set to achieve sub-lattice imaging. For example here, we are trying to explore the possibility to create a digital detector response function that can amplify signals of one sub-lattice over the other.

2.2 Digital detector response function design and mathematical formulation

The most simple way to create the detector response function for selecting one set of sub-lattice is through crystal division. It can be formulated below,

Let's denote the diffraction pattern as I(x,y,kx,ky). x, and y are the spatial coordinate within one unit cell. kx, and ky are the reciprocal space coordinates. The full crystal CBED pattern is defined as:

$$I_{cyrtal}(kx, ky) = \frac{\sum_{x,y} I(x, y, kx, ky)}{\sum_{x,y} 1}$$

Let's define a set of sub-lattice and their coordinates within a unit cell is x_sub, y_sub. The sub-lattice CBED pattern is:

$$I_{sub}(kx, ky) = \frac{\sum_{x_{sub}, y_{sub}} I(x, y, kx, ky)}{\sum_{x_{sub}, y_{sub}} 1}$$

Then, we define a ratio map for the sub-lattice

$$R_{sub}(kx, ky) = \frac{I_{sub}(kx, ky) + 1}{I_{crystal}(kx, ky) + 1}$$

Here the offset by one is to prevent the dividing by zero problem. Then, the detector response function can be defined as:

$$D(kx, ky) = \begin{matrix} 1 \; if \; R_{sub}(kx, ky) \geq threshold \\ 0 \; if \; R_{sub}(kx, ky) < threshold \end{matrix}$$

2.3 Digital detector response function for Sr, Ti-O, and Oxygen sub-lattices in [001] $SrTiO_3$

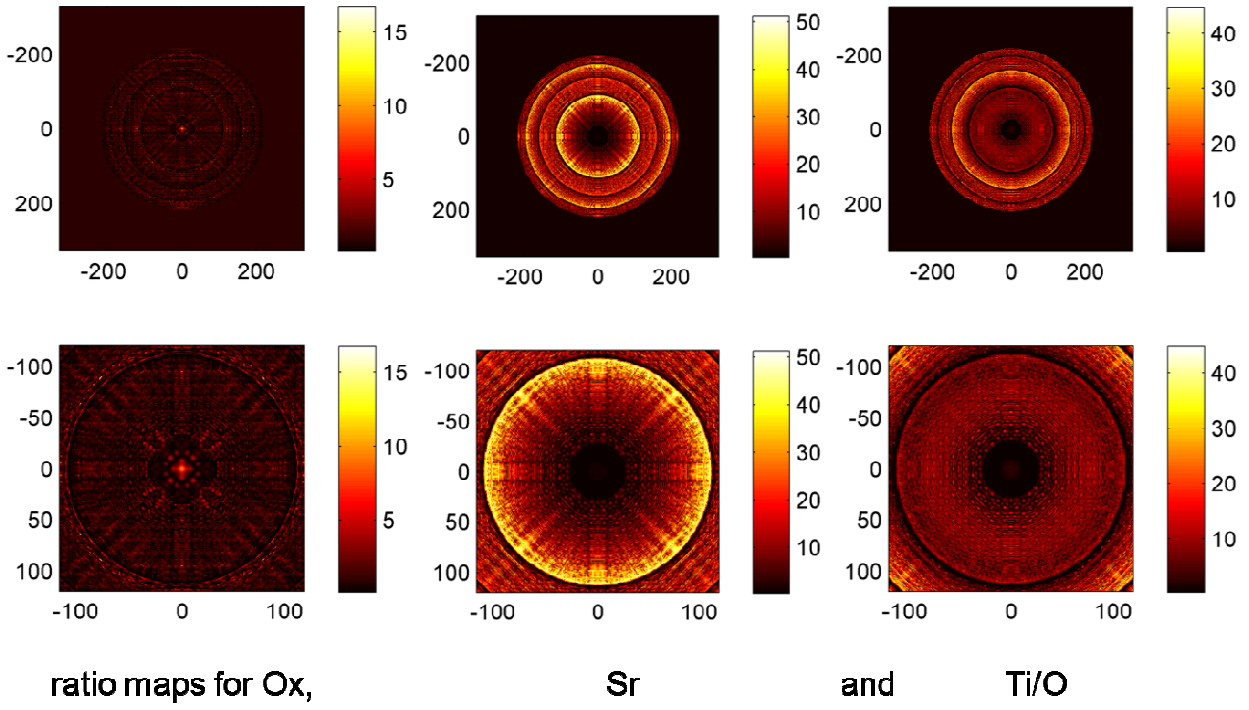

Figure 12. The sub-lattice ratio maps for Sr, Ti-O, and Oxygen sub-lattices in [001] $SrTiO_3$

As shown in Figure 12. The ratio maps for Ox, Sr, and Ti-O sub-lattices are significantly different, this gives us confidence that this could map the specified sub-lattices in real space by translating he ratio maps into the detector functions in Figure 13.

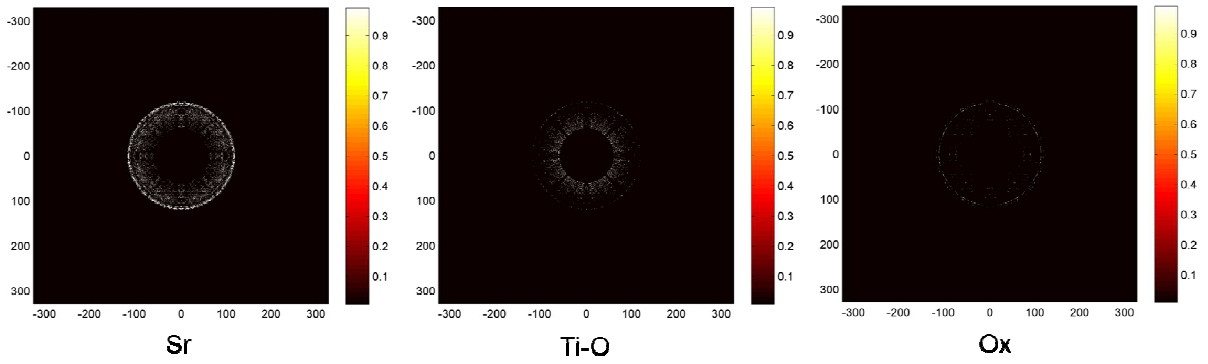

Figure 13. The sub-lattice detector response functions for Sr, Ti-O, and Oxygen sub-lattices in [001] $SrTiO_3$.

2.3 Sub-lattice imaging through engineered digital detector response function

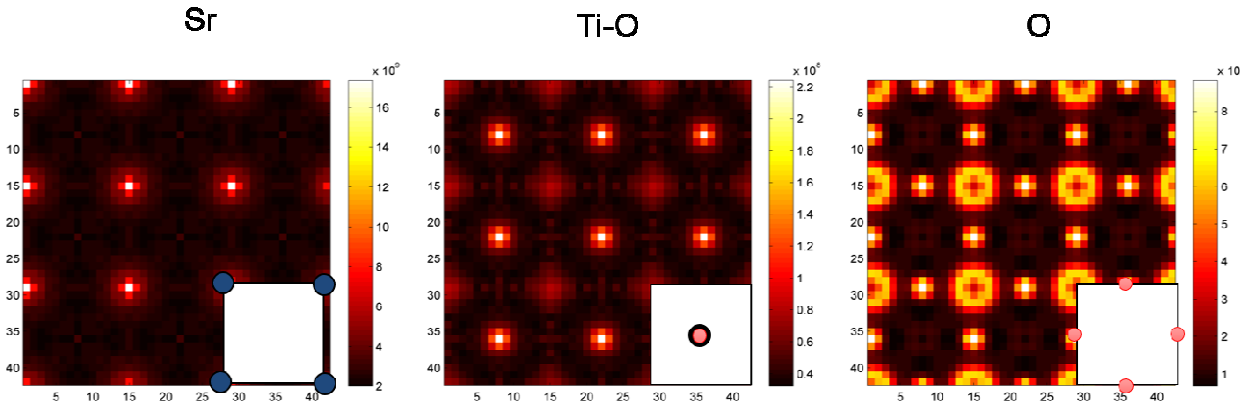

Figure 14. Real real space map rendered through applying the sub-lattice detector response function extracted in Figure 13.

As shown in Figure 14, Sr sub-lattice can be mapped out the best. The signals are concentrated on where the Sr columns ar e sitting at. The Ti sub-lattice has a small contribution from the Sr lattice likely because Sr is a much heavier scatterer. As for Ox sub-lattice, we see a donut shape feature show up around the site of the Sr column.

2.4 Conclusions

Overall speaking, the heaviest scatterer, Sr, can be mapped out very well using our crystal division method. However, other machine learning or optimization methods are needed to improve the sub-lattice differentiation of the lighter columns.

References

1. Muller, D.A., *Structure and bonding at the atomic scale by scanning transmission electron microscopy.* Nature Materials, 2009. **8**(4): p. 263-270.

2. Yu, Z.H., D.A. Muller, and J. Silcox, *Study of strain fields at a-Si/c-Si interface.* Journal of Applied Physics, 2004. **95**(7): p. 3362-3371.

3. Dekkers, N.H. and H.D. Lang, *DIFFERENTIAL PHASE-CONTRAST IN A STEM.* Optik, 1974. **41**(4): p. 452-456.

4. Chapman, J.N., I.R. McFadyen, and S. McVitie. *MODIFIED DIFFERENTIAL PHASE-CONTRAST LORENTZ MICROSCOPY FOR IMPROVED IMAGING OF MAGNETIC-STRUCTURES*. 1990: Ieee-Inst Electrical Electronics Engineers Inc.

5. Caswell, T.A., et al., *A high-speed area detector for novel imaging techniques in a scanning transmission electron microscope.* Ultramicroscopy, 2009. **109**(4): p. 304-311.

6. Kirkland, E.J. and M.G. Thomas, *A high efficiency annular dark field detector for STEM.* Ultramicroscopy, 1996. **62**(1-2): p. 79-88.

7. KILVINGTON, A.I., C.A. BAKER, and P. ILLINES, *R.EFLECTIVE COVERINGS FOR SCINTILLATION COUNTERS.* NUCLEAR INSTRUMENTS AND METHODS 1970. **80**: p. 177-178.

8. Vernon, W., et al., *First resutls from the 128x128 pixel mixed-mode Si X-ray detector chip.* SPIE optics and photonics conference, 2007.